

## SMILES ice cloud products

L. Millán,<sup>1</sup> W. Read,<sup>1</sup> Y. Kasai,<sup>2</sup> A. Lambert,<sup>1</sup> N. Livesey,<sup>1</sup> J. Mendrok,<sup>2,3</sup> H. Sagawa,<sup>2</sup> T. Sano,<sup>4</sup> M. Shiotani,<sup>5</sup> and D. L. Wu<sup>6</sup>

Received 17 October 2012; revised 4 March 2013; accepted 7 March 2013; published 21 June 2013.

[1] Upper tropospheric water vapor and clouds play an important role in Earth's climate, but knowledge of them, in particular diurnal variation in deep convective clouds, is limited. An essential variable to understand them is cloud ice water content. The Japanese Superconducting Submillimeter-Wave Limb-Emission Sounder (SMILES) on board the International Space Station (ISS) samples the atmosphere at different local times allowing the study of diurnal variability of atmospheric parameters. We describe a new ice cloud data set consisting of partial Ice Water Path and Ice Water Content. Preliminary comparisons with EOS-MLS, CloudSat-CPR and CALIOP-CALIPSO are presented. Then, the diurnal variation over land and over open ocean for partial ice water path is reported. Over land, a pronounced diurnal variation peaking strongly in the afternoon/early evening was found. Over the open ocean, little temporal dependence was encountered. This data set is publicly available for download in HDF5 format.

**Citation:** Millán, L., W. Read, Y. Kasai, A. Lambert, N. Livesey, J. Mendrok, H. Sagawa, T. Sano, M. Shiotani, and D. L. Wu (2013), SMILES ice cloud products, *J. Geophys. Res. Atmos.*, 118, 6468–6477, doi:10.1002/jgrd.50322.

### 1. Introduction

[2] Clouds are the major source of uncertainty in the estimates of the radiative forcing of climate [IPCC, 2007]. Clouds have both a heating and cooling effect on the Earth-atmosphere system: a heating effect through absorption and reemission of thermal infrared radiation emitted below them, and a cooling effect through reflection of incoming sunlight. Whether the net effect is one of warming or cooling depends on many complex factors, such as cloud's altitude, horizontal extent, composition (ice versus liquid water), microphysical properties, as well as the incoming solar radiation. Particularly, the amount of ice clouds differ by orders of magnitude among climate models [e.g., Stephens *et al.*, 1990; Penner, 2004; Li *et al.*, 2005; Jiang *et al.*, 2012; Li *et al.*, 2012] due to poorly resolved dynamic processes that generate the ice clouds, the accuracy of the water vapor transport to and within the upper troposphere, the microphysical formation mechanism of the ice particles [Del Genio, 2001], and the assumptions made about the ice sedimentation rates [Wilson, 2000; Mitchell *et al.*, 2008].

A review of the importance of ice crystals properties to climate prediction can be found in Baran [2012].

[3] Visible and infrared observations of clouds have provided vast amount of information on cloud properties; however, these techniques are limited to thin clouds or to the topmost layer of clouds, hence, cannot provide much needed information on the internal structure of clouds, such as the cloud ice mass. Passive submillimeter satellite observations can penetrate through most ice clouds and provide cloud ice mass information primarily through scattering in the Rayleigh-Mie region so that cloud temperature, cloud and surface emission, and multiple scattering that affect other remote sensing techniques are relatively unimportant [e.g., Evans *et al.*, 1998; Wu *et al.*, 2005; Eriksson *et al.*, 2007; Buehler *et al.*, 2007; Jiménez *et al.*, 2007; Buehler *et al.*, 2012]. Furthermore, active instruments have been proven to measure cloud ice mass with high vertical resolution [Stephens *et al.*, 2002; Winker *et al.*, 2009; Kumagai *et al.*, 2003].

[4] Measurements from the Earth Observing System (EOS) Microwave Limb Sounder (MLS), the CloudSat - Cloud Profiling RADAR (CPR) and the CALIPSO - Cloud Aerosol Lidar with Orthogonal Polarization (CALIOP) instruments (for more details about these instruments, see section 3) have provided a wealth of information about the atmospheric Ice Water Content (IWC) serving as guidance to improve the simulations and predictions of cloud-related processes [e.g., Li *et al.*, 2005, 2012]. However, these instruments are all in the “A-train” constellation of satellites and observe essentially the same air mass within minutes of each other, conveying information only at two fixed local times each orbit ( $\sim 1:45$  A.M./P.M.); the “A-train” constellation of satellites cannot resolve the diurnal cycle. In this study, we introduce the new partial Ice Water Path

<sup>1</sup>Jet Propulsion Laboratory, California Institute of Technology, Pasadena, California, USA.

<sup>2</sup>National Institute of Information and Communications Technology (NICT), Koganei, Tokyo, Japan.

<sup>3</sup>Luleå University of Technology, Kiruna, Sweden.

<sup>4</sup>Japanese Aerospace Exploration Agency, Cho-fu, Tokyo, Japan.

<sup>5</sup>Kyoto University, Kyoto, Kyoto, Japan.

<sup>6</sup>NASA Goddard Space Flight Center, Greenbelt, Maryland, USA.

Corresponding author: L. Millán, Jet Propulsion Laboratory, California Institute of Technology, Pasadena, CA, USA. (lmillan@jpl.nasa.gov)

©2013. American Geophysical Union. All Rights Reserved.  
2169-897X/13/10.1002/jgrd.50322

(pIWP) and IWC observations from the Superconducting Submillimeter-Wave Limb-Emission Sounder (SMILES).

[5] SMILES was launched in September 2009 and successfully attached to the front-side of the International Space Station (ISS). SMILES measured, on a time sharing basis, two of three frequency bands: 624.32–625.52 GHz (band A), 625.12–626.32 GHz (band B), and 649.12–650.32 GHz (band C) from October 2009 to April 2010 [Kikuchi *et al.*, 2010]. During this period, the SMILES antenna, with an instantaneous field of view of  $0.09^\circ$  ( $\sim 3$  km at limb tangent) [Manabe *et al.*, 2008, 2010], scanned the Earth's limb covering tangent heights between 10 and at least 60 km about 1600 times per day, with the objective of measuring emission lines of atmospheric minor constituents such as  $O_3$  and its isotopes, HCl, ClO,  $HO_2$ , BrO, and  $HNO_3$ . The radiation received was down-converted using two 4 K cooled Superconductor-Insulator-Superconductor (SIS) mixers, and spectra were recorded by two sets of acousto-optical spectrometers (AOS). SMILES data has a latitudinal coverage from  $65^\circ N$  to  $38^\circ S$  covering all the local solar times. SMILES, as a payload of the ISS, which is in a  $51.6^\circ$  inclined orbit, made observations at local times that drifted  $\sim 20$  min earlier each day covering the entire diurnal cycle in a period of about 2 months. These measurements provide unique valuable information to potentially enable improvements in model representations of diurnal cycles in convection, known to be deficient in many scenarios [e.g., Tian *et al.*, 2004; Lee *et al.*, 2008].

[6] This paper is structured as follows. First, the retrieval methodology used to convert the SMILES measurements to relative humidity, IWC, and pIWP is presented followed by an analysis of the precision and systematic uncertainties. Then, we compare this new data to the MLS, CloudSat-CPR, and CALIPSO-CALIOP data sets. Finally, the cloud pIWP diurnal variation derived from SMILES is explored.

## 2. Retrieval Approach

[7] The fundamental measurement from which ice cloud retrievals derive is the cloud-induced radiance ( $T_{cir}$ ). This quantity is defined as the difference between the measured radiance and the expected clear-sky radiance. Once the clear-sky radiance is known, we use simulated  $T_{cir}$ -pIWP and  $T_{cir}$ -IWC linear relationships to map it either to pIWP or IWC, respectively. Figure 1 outlines the SMILES ice cloud retrieval algorithm.

[8] The estimation of the clear-sky radiances starts with an inversion of SMILES spectra to determine the limb tangent pressure as well as the concentrations of  $O_3$  and HCl. The retrieval uses the optimal estimation technique as described by [Rodgers, 2000] using the hydrostatic equation as a constraint (in a similar manner as the retrieval described by [Livesey *et al.*, 2006]). The temperature information is taken from GEOS-5 [Rienecker *et al.*, 2008], and the a priori for the  $O_3$  and HCl is taken from the closest, geographically and in time, Microwave Limb Sounder (MLS) [Waters *et al.*, 2006] scan (for more information on this data set, see section 3). Their respective a priori precision, their assumed random error, are 5 ppmv and 1 ppbv. GEOS-5 temperature, MLS  $O_3$ , and HCl are chosen as a priori to use the most realistic atmospheric representation available.

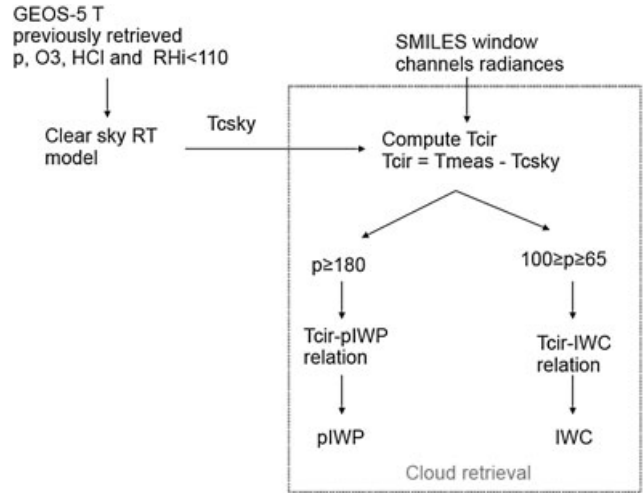


**Figure 1.** SMILES cloud ice retrieval scheme where  $T$ ,  $p$ ,  $O_3$ , HCl and RH are temperature, pressure, ozone and hydrogen chlorine and where  $T_{csky}$ ,  $T_{cir}$  and  $T_{meas}$  are the clear-sky radiances, the cloud induced radiances and the SMILES measured radiances, respectively.

[9] This inversion is performed in two phases. The first phase estimates these parameters over a subset of the vertical range with the purpose of deriving a height offset to mitigate the ISS pointing uncertainty. The subset radiances used are selected to have a minimum strength of 1 K and a maximum strength of 60 K to ensure that they are optically thin. The second phase uses the updated pointing heights and repeats the whole retrieval, now between 18 and 55 km. The reason for the two-phase strategy is to ensure that the vertical range of radiances used for the pressure retrieval is consistent from scan to scan.

[10] Relative humidity (RH) is inverted with a similar algorithm to that described by Read *et al.* [2001]. In this algorithm, relative humidity is retrieved directly from the water vapor continuum, modifying the water vapor Jacobians using the Goff-Gratch function [List, 1951], an empirical function that estimates the saturation water vapor pressure at a given temperature. Once relative humidity is known, the clear-sky radiance can be computed simulating the limb radiances using GEOS-5 temperature, the pressure, HCl, and  $O_3$  retrieved values, as well as the retrieved relative humidity in values of up to 110% (i.e., any value greater than 110% is truncated). This RH threshold was previously used by Wu *et al.* [2005] and represents the uncertainty of RH. The most useful frequencies to derive the clear-sky radiance are those away from strong spectral lines, the so-called “window channels.” Figure 2 shows the position of the window channels used in this study. These window channels were selected avoiding the influence of overlapping species and trying to find the most optically thin radiance at 100 hPa; that is to say, where its optical depth is the smallest. Brightness temperature was computed inverting the Plank function.

[11] Figure 3 shows a typical example of the measured window channel radiance and the  $T_{cir}$  (the difference between the measured radiance profile and its corresponding clear-sky radiance). As shown, most of the points tend to bundle around zero  $T_{cir}$  with a  $\sim 2$  K variation. Lines

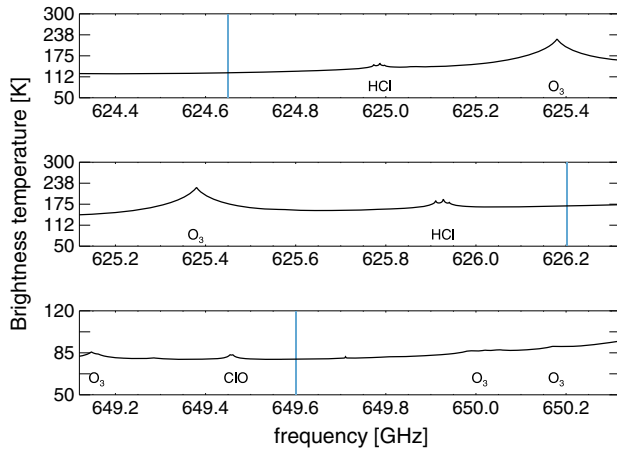


**Figure 2.** Simulated limb radiances at 100 hPa for the SMILES bands A, B, and C (top, middle and bottom panels, respectively). The molecules responsible for most of the prominent emissions are labeled. Blue lines show the window channels used in this study, each of them being 2 MHz wide.

representing the  $3\sigma - 2\sigma$  deviation are overlaid as an indication of the clear-sky limit. Points that fall outside this region are cloud occurrences. The  $3\sigma - 2\sigma$  screening method is explained in detail by [Livesey *et al.*, 2011]. In short, Tcir data was averaged iteratively rejecting  $2\sigma$  outliers each iteration. After convergence, the  $3\sigma$  threshold determined if a Tcir measurement is statistically significant. In other words, Tcir must be greater than the mean +  $3\sigma$  to be considered as a significant cloud hit.

[12] Figure 3 shows that clouds can enhance or reduce radiances with respect to the clear-sky radiance mostly depending on the tangent height measured, with positive Tcir at high altitudes and negative Tcir at low altitudes. This can be understood assuming a thin cloud acts only as a scattering medium, reflecting the negligible radiance from above the cloud (cosmic background radiation plus the downward radiation), and the radiance from below the cloud (the upward radiation) into the line of sight. Under this assumption, the measured radiance under the presence of this particular cloud will be almost constant, probably around 101 K (a simple average of the 200 K from the surface and the  $\sim 3$  K from the cosmic background radiation) irrespective of the cloud height. Hence, at high altitudes, where the clear-sky radiance is smaller than the cloud radiance, the cloud will produce a positive Tcir, while at low altitudes the clear-sky radiance is greater than the cloud radiance producing a negative Tcir. In the interim altitudes, where the cloud radiance is similar to the clear-sky radiance, the lack of contrast between the two makes any ice cloud information difficult to obtain.

[13] At low tangent heights, in this case for pressures larger than  $\sim 200$  hPa (approximately around 12.5 km), the atmosphere becomes opaque (i.e., its optical depth becomes greater than 1) before the line of sight reaches the limb; therefore, although the tangent height of the measurement might be close to the surface, the actual cloud signal originates higher up in the atmosphere. In this scenario, vertically scanning does not provide much vertically resolved

information on the cloud. Rather, each limb scan measures a different location thereby trading vertical sampling for horizontal sampling much like a nadir instrument viewing side to side sweeping. As such, negative Tcir conveys information that is more related to the pIWP, the ice partial column along the line of sight, than IWC, the amount of ice per unit volume at the measured altitude. At higher tangent heights, in this case for pressures smaller than 100 hPa, where the atmosphere is optically thin, vertically scanning provides vertically resolved cloud information physically related to IWC. At the intermediate pressure levels, between 180 and 100 hPa, the clouds lack contrast with the clear-sky background, and, as explained before, there is no cloud information in the measured radiance.

[14] Positive and negative Tcir have been mapped to IWC or pIWP, respectively, using radiative transfer simulations described in the following section. In summary, the entire SMILES data set has been processed: IWC, the density of ice at the measured tangent pressure, is available between 100 to 70 hPa; and pIWP, the partial amount of ice along the SMILES line of sight above around 12.5 km is available for pressures greater than 180 hPa.

## 2.1. Radiative Transfer Simulations

[15] Once the SMILES Tcir are known, the next step to generating the ice cloud products is to use Tcir-pIWP and Tcir-IWC relationships derived using simulations from the 2-D Cloud-Sky Radiative Transfer (RT) model, a 2-D version of the model described by Wu [2006] and Wu *et al.* [2008]. This model assumes spherical ice particles, computes the absorption and scattering cloud volume

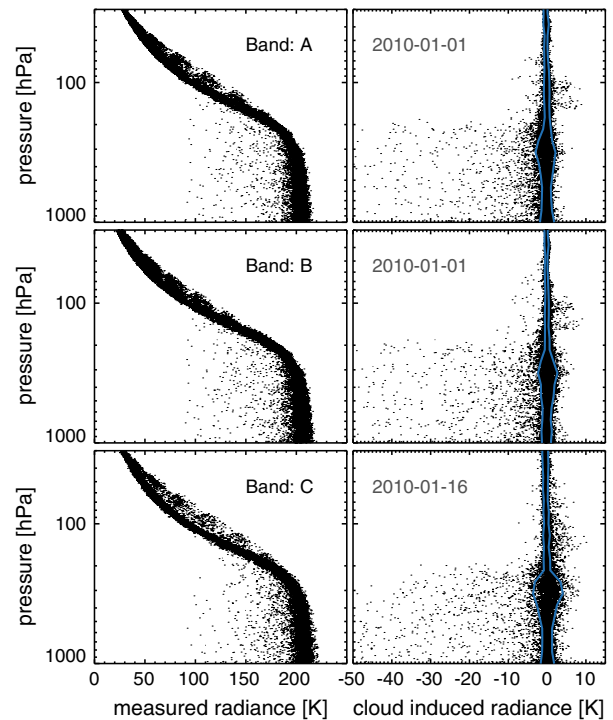


**Figure 3.** Measured radiance from SMILES band A, B, C (left) and retrieved  $T_{cir}$  (right). Most points outside the blue lines are cloud detections while points between them are clear-sky or undetectable clouds.

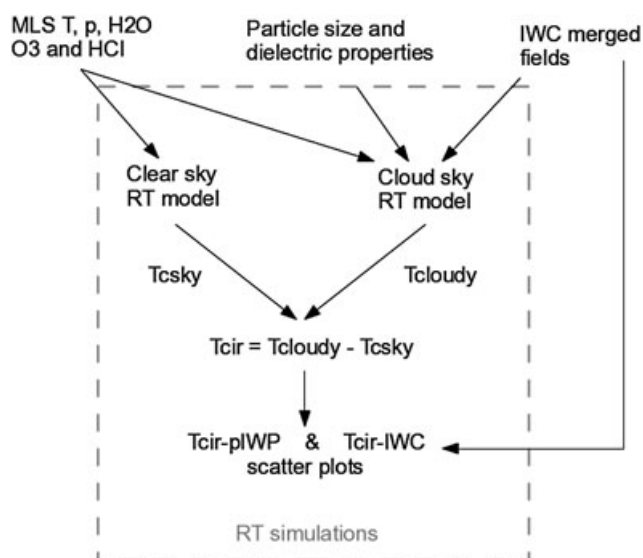


**Figure 4.** SMILES cloud ice RT simulations scheme where  $T$ ,  $p$ ,  $O_3$ ,  $HCl$  and  $RHi$  are temperature, pressure, ozone and hydrogen chlorine and where  $T_{csky}$  and  $T_{cloudy}$  are the simulated clear-sky and cloudy radiances, respectively.

coefficients and phase functions assuming single scattering properties, and then solves the RT equation (neglecting polarization) iteratively (following [Wilheit *et al.*, 1982; Yeh *et al.*, 1990]) to include multiple scattering effects. Figure 4 shows an outline of these simulations.

[16] These simulations were performed on merged daily IWC fields from the CloudSat-CPR and the CALIPSO-CALIOP (for more information of these data sets see section 3). These merged fields were simply the largest IWC value between the two data sets at any given pressure level reported in a pressure grid of 24 levels per decade with an along-track resolution of half degree. This simple method allows us to exploit the sensitivity of CALIPSO-CALIOP

for small ice particles that CloudSat-CPR cannot detect, as well as the higher dynamic range of CloudSat at IWC concentrations where CALIPSO-CALIOP measurements saturate. The goal was to produce a set of simulations which had realistic IWC concentrations and heterogeneity from which to produce  $T_{cir}$ -IWP and  $T_{cir}$ -IWC correlations. The atmospheric temperature and concentrations were taken from the nearest MLS profiles, and the particle size distribution (PSD) parametrization used was the McFarquhar and Heymsfield [1997] parametrization derived from measurements during the Central Equatorial Pacific Experiment Campaign. Although, this PSD may be skewed due to impact shattering on the housing of probes [Korolev *et al.*, 2011], and as shown by Field *et al.* [2006], this could result in an overestimation of the ice water content by the mass diameter relationship of around 20%–30%, this PSD was used to be consistent with the MLS and CloudSat retrieval algorithms. Note that these simulations take into account the SMILES antenna response function.

[17] For each cloudy scene, the RT model was run under clear-sky conditions to compute the corresponding clear-sky radiances. Then, the pairing of the known pIWP or IWC and the  $T_{cir}$  was used to derive the  $T_{cir}$ -pIWP and  $T_{cir}$ -IWC relationships. As an example, Figure 5 shows a typical  $T_{cir}$ -pIWP scatter plot at 1000 hPa for simulations of band A B, and C, using data corresponding to 15 March 2010. In addition, a linear fit is shown. This fit is used to characterize the  $T_{cir}$ -pIWP relationship at this tangent pressure level and for this particular day; the linear Pearson correlation coefficient and the slope 1-sigma uncertainty for the three bands was around  $-0.95$  and  $0.016$ , respectively. Scatter plots at different tangent pressure levels were analyzed to find this relationship at different tangent pressures. This analysis was carried-out for  $\sim 30$  days sparsely distributed throughout the entire SMILES mission, and no seasonal dependence was found.

[18] Given the lack of seasonality, an average of the daily corresponding fits, for each pressure level, and their standard deviation were used to characterize the data. Figure 6

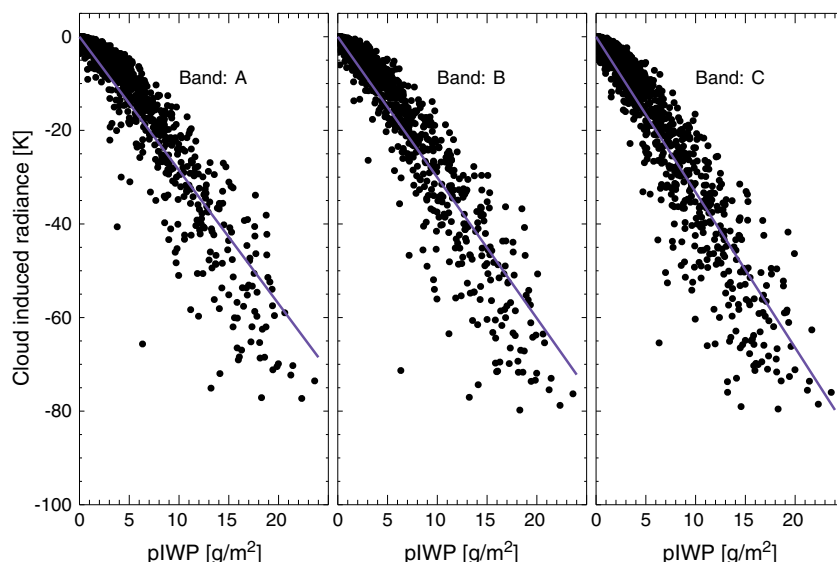


**Figure 5.** Scatter plot of simulated  $T_{cir}$  versus pIWP for bands A, B and C at 1000 hPa (black dots) for 15 March 2010. The purple line shows a linear fit of the data.

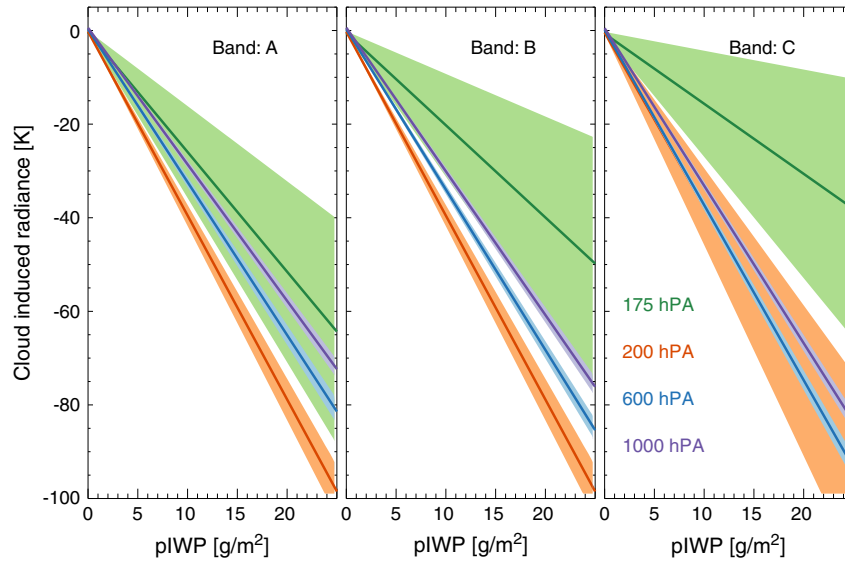


**Figure 6.** Final bands A, B and C simulated Tcir-pIWP relationship for different pressure levels built using a conglomeration of the linear fits found in 30 days of simulations spread throughout the SMILES mission. The pressure levels are color coded, a paler color shows the standard deviation at that particular level.

displays the mean value and standard deviation for several pressure levels. As the pressure decreases, the standard deviation increases; above 180 hPa, the standard deviation is so big that no useful relationship can be found. These values were used to map the measured Tcir onto the corresponding pIWP; the standard deviation of these fits is a measure of the uncertainty in pIWP due to vertical and along-track inhomogeneities as well as the pIWP missing contributions that are below the penetration depth of the signal.

[19] A similar analysis was performed to find relationships between Tcir and IWC. In this case, the Tcir-IWC relationships were restricted to Tcir measured at tangent pressures between 100 and 70 hPa, where most of the Tcir are positive. Furthermore, the Tcir used were not a single measurement but rather the mean value of a defined atmospheric volume (275 km along the track and 3.3 km in the vertical). As with pIWP, no seasonality was found during the analysis of the  $\sim 30$  days spread throughout the entire SMILES mission. Hence, as before, for each pressure level, an average of the corresponding fits and their standard deviation was used to characterize the data. In this case, the spread is caused by cloud inhomogeneities along the line of sight.

## 2.2. Tcir Error Assessment

[20] The total error in the calculated Tcir is given by a sum of random and systematic errors. The random errors are determined by the noise in the SMILES measurements, in this case less than 0.7 K for a single AOS channel [Kikuchi *et al.*, 2010]. And the systematic errors arise from uncertainties in the forward model, instrumental issues, and retrieval approximations.

[21] The random errors plus some systematic errors in the derived Tcir can be estimated empirically from the data using the  $3\sigma$ - $2\sigma$  method used to find the clear-sky limit. The systematic errors captured in this error estimate are the uncertainties in the temperature and in the gas concentra-

tions retrievals used as part of the Tcir calculation. Note that other sources of systematic errors affecting the Tcir estimates, such as spectral and radiometric calibration issues, and pointing deficiencies, still need to be investigated, but are presumably negligible compared with the rest of the systematic uncertainties (see section 2.3). Figure 7 shows the Tcir bias and precision for a typical day. As shown, the bias (the mean) is less than 0.5 K while the precision ( $1\sigma$  variation) is around 1 K for pressure levels between 1000 and 200 hPa, and less than 0.5 K for pressures smaller than 200 hPa.

[22] Figure 8 shows how these errors propagate into the retrieved pIWP and IWC for band A (bands B and C are similar). These propagations were performed updating

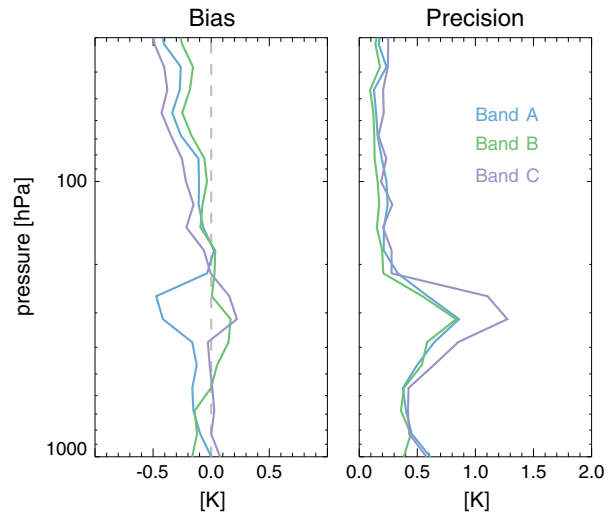


**Figure 7.** Empirically derived Tcir bias and precision for each SMILES band for a typical day as function of tangent pressure. The bias and precision for each band are color coded.



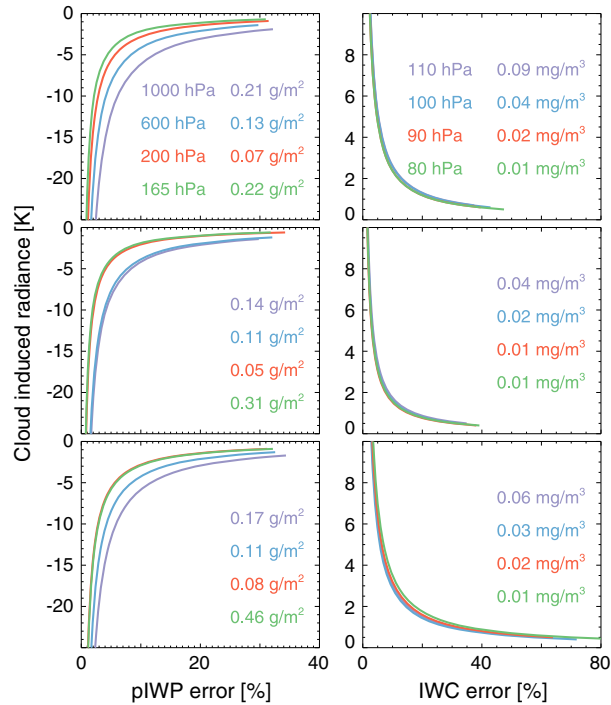


**Figure 8.** pIWP and IWC percentage errors for SMILES bands A,B and C due to the empirically derived Tcir bias and precision for different tangent pressures. The errors are only shown for Tcir values greater than the clear-sky limit determined for each tangent pressure. For each pressure level, the absolute error is presented to give a sense of the detectability thresholds.

the Tcir-pIWP and the Tcir-IWC relationships discussed in section 2.1. For pIWP, the error varies from less than  $\sim 10\%$  to up to  $40\%$ . For IWC, the error varies from less than  $\sim 10\%$  to up to  $80\%$ , depending on the induce Tcir value. Maximum relative errors occur when the Tcir approaches zero, that is to say, for cloud free scenes. The absolute errors give a sense of the minimum ice detection threshold and are also specified in Figure 8.

### 2.3. pIWP and IWC Systematic Uncertainties

[23] In addition to the errors discussed in the previous section, the total error in pIWP and IWC needs to include more systematic uncertainties, such as cloud inhomogeneity, water vapor spectroscopy uncertainties, uncertainties due to different PSDs, and uncertainties in the particle shape. The impact of these systematic uncertainties are summarized in Table 1.

[24] The uncertainty given by cloud inhomogeneity was estimated from the standard deviation of the fits discussed in section 2.1. These fits were obtained using realistic distributions of ice clouds data from CloudSat-CPR and CALIPSO-CALIOP and, as such, the standard deviation in these fits represent the variation due to cloud spatial variability as well as temporal variability, at least in the sense that several days were used to estimate those fits.

[25] To investigate the error associated with the uncertainties in the water vapor spectroscopy, its parameters were perturbed by  $30\%$  and the Tcir-pIWP and Tcir-IWC relationships were recomputed. The errors were found comparing the Tcir-pIWP and Tcir-IWC relationships found using the perturbed spectroscopy parameters against the unperturbed PSD.

[26] Furthermore, the Tcir-pIWP and Tcir-IWP relationships were recomputed using different PSD parameterization schemes: the one given by *Field et al.* [2007] and those described by *Donovan and Lammeren* [2002] and *Heymsfield et al.* [2002]. When using the first two, the particle maximum dimension was converted to the mass equivalent diameter using the mass-diameter relationship described by *Cotton et al.* [2012]. Unfortunately, the *Donovan and Lammeren* [2002] and *Heymsfield et al.* [2002] parameterization schemes are limited to temperatures greater than  $-50^\circ\text{C}$  and therefore the errors associated to different particle size distribution can only be computed for tangent pressures between 1000 to  $\sim 220$  hPa. This pressure range only matches the pressure levels of the Tcir-pIWP relationships, so, for these PSDs, their corresponding error was only computed for pIWP.

[27] To investigate the uncertainty due to particle shape or habit, a forward model capable of simulating polarized scattered radiance is needed. That is to say, to propagate the four elements of the Stokes vector through the appropriate extinction and scattering phase matrices. For instance, the Atmospheric Radiative Transfer Simulator (ARTS) [*Buehler et al.*, 2005; *Eriksson et al.*, 2011a] could be coupled with a T-matrix code (such as the one described by *Mishchenko and Travis* [1998]), to estimate this error; however, this is outside the scope of this study. Yet, as discussed by *Eriksson et al.* [2011b], an instrument that covers the left-and-right-hand circular components of the polarization effects, such as SMILES, should be less affected by the naturally occurring cloud complex ice particle shapes. Considering this, we assume an error of  $20\%$  for this uncertainty, as derived by *Wu et al.* [2008] for the MLS instrument (see section 3 for more details about this instrument). As discussed by *Eriksson et al.* [2011b], as the MLS instrument measures the horizontal and vertical linear components,

**Table 1.** Estimated Systematic Uncertainties for pIWP and for IWC

	Ptan [hPa]	Cloud Inhomogeneity (%)	H <sub>2</sub> O Spectroscopy (%)	Other PSDs (%)	Particle Shape (%)	Total (%)
IWC	70	42	10	29	20	57
	80	36	11	26	20	51
	90	19	26	38	20	54
	100	17	36	29	20	53
pIWP	180	7	3	69	20	72
	220	5	1	107 <sup>a</sup>	20	109
	600	3	2	54 <sup>a</sup>	20	57
	1000	3	2	46 <sup>a</sup>	20	50

<sup>a</sup> Mean error of the PSDs discussed in the text.

it should be more affected by the non-spherical particle shapes than SMILES. Presumably, even considering that the SMILES window channels will be more sensitive to smaller particles, which have larger polarization effects, our estimate is in the right magnitude.

### 3. Comparison With Other Data Sets

[28] Comparisons of a monthly means were made with those of the MLS, CloudSat-CPR and CALIPSO-CALIOP instruments.

[29] MLS measures thermal microwave limb emission in five spectral regions from 115 GHz to 2.5 THz, including a 640 GHz region with similar coverage as SMILES. It was launched in July 2004 on board the Aura spacecraft. MLS scans the limb from the ground to about 95 km roughly 3500 times per day. It covers between 82°S and 82°N providing near global coverage. At most latitudes, about half of these measurements are made around 1:45 P.M. and the other half around 1:45 A.M., except around the poles where the measurements change between daytime and nighttime conditions or vice versa [Waters *et al.*, 2006].

[30] Because the penetration depth of passive sensors, such as SMILES and MLS, depends on the frequency used, in this study, we consider the MLS pIWP (version 3.3) from the 640 GHz radiometer to better match the SMILES observations (the standard MLS pIWP have an altitude base of  $\sim 6$  km while the MLS-640 GHz and SMILES pIWP have one at  $\sim 12.5$  km). For the IWC comparisons, we show both the standard and the MLS-640 GHz products to compare the validated MLS-IWC product as well as the IWC derived with SMILES-like frequencies. Note that, although MLS-640 GHz and SMILES pIWP and IWC are derived from similar frequencies, they used different retrieval algorithms. In addition, the MLS-640 GHz products do not have a published assessment of their quality.

[31] CloudSat is the first spaceborne Cloud Profiling RADAR (CPR) launched in April 2006 [Stephens *et al.*, 2002]. It measures the power backscattered by clouds as a function of distance. This satellite orbits in formation minutes ahead of the Aura spacecraft. The effective dimensions of a single measurement are approximately 1.3 km cross-track and 1.7 km along-track. Each CPR profile consists of 125 levels that are  $\sim 240$  m apart from the ground to  $\sim 28$  km, although the CPR resolution is approximately 500 m. Here we use the IWC profiles from the 2B-CWC-RO R04 product.

[32] The Cloud-Aerosol Lidar with Orthogonal Polarization (CALIOP) instrument is a two wavelength polarization sensitive LIDAR that provides high resolution profiles of aerosols and clouds [Winker *et al.*, 2009]. It was launched in April 2006, alongside CloudSat, on board the CALIPSO platform. This platform orbits in formation with Aura, as CloudSat also does.

[33] pIWP were derived from the CloudSat-CPR and CALIPSO-CALIOP IWC data sets assuming a base altitude of 12.5 km to match the penetration depth of the passive sensors, the altitude at which most atmospheric scenarios the optical depth window channels become optically thick.

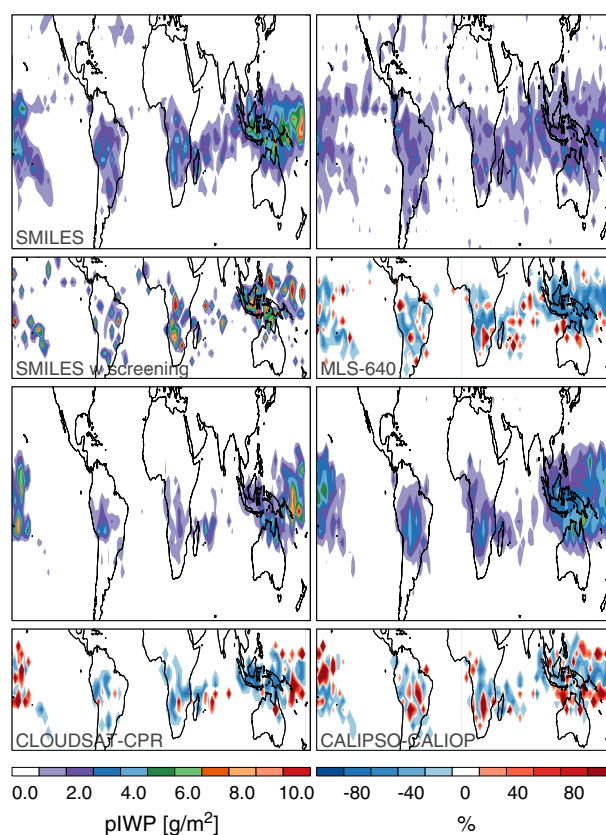


**Figure 9.** SMILES (bands A, B and C), MLS-640 GHz, CloudSat and CALIPSO pIWP monthly mean for January 2010 with and without diurnal screening. CloudSat and CALIPSO pIWP maps correspond to a partial column above 12.5 km, approximately the penetration depth of SMILES and MLS-640 GHz. Also, the percentage difference between SMILES (without diurnal screening) and the other data sets is shown. Due to the diurnal variation of this parameter, and due to the instrument dependent particle size sensitivity, exact agreement is not expected.

#### 3.1. Geographical Distribution

[34] Figure 9 shows a monthly mean of pIWP for January 2010 for SMILES, MLS, CloudSat-CPR, and CALIPSO-CALIOP data. For SMILES, two monthly means are shown, one which represents a simple average of all the data (a merge of the three bands) with no diurnal screening, and one showing the SMILES measurements made around 1:45 A.M. and 1:45 P.M. Figure 9 also displays the percentage difference between the data sets. To compute it, all the SMILES data were used in order to maximize the number of SMILES points per latitude-longitude bin. Hence, direct comparison with the other measurements needs to keep diurnal sampling issues in mind. As can be seen, the four data sets show relatively high values around the inter-tropical convergence zone (ITCZ), agreeing well in the pIWP geographical pattern. The data sets do not agree entirely in magnitude, but this is expected; the instruments are sensitive to different particle sizes and different assumptions are made in each retrieval. Also, cloud inhomogeneity, variability, and the different sampling of the diurnal cycle, will all contribute to disagreement in pIWP. In general, SMILES pIWP

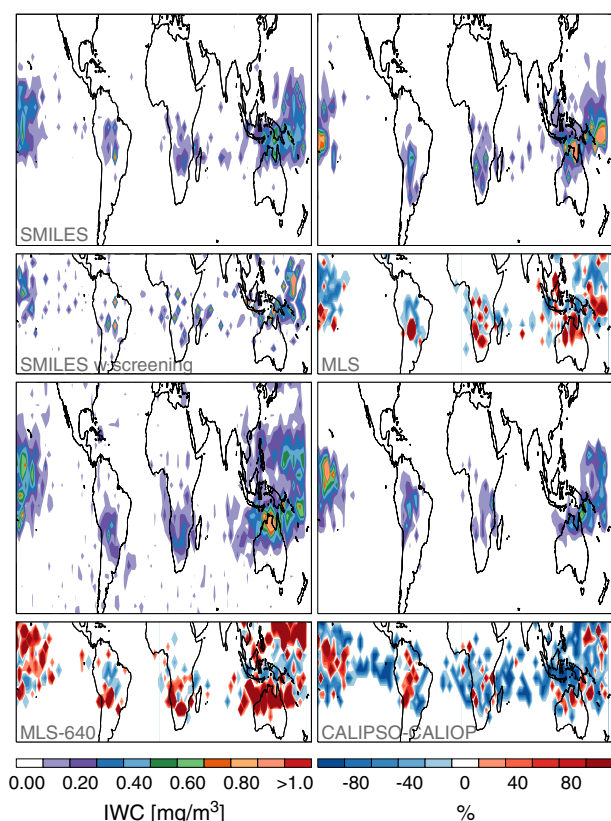


**Figure 10.** Same as Figure 9, except for IWC at 100 hPa.

lies between 100% smaller and 100% greater than MLS-640 GHz, CloudSat-CPR, and CALIPSO-CALIOP data, depending on location.

[35] Figure 10 shows a monthly mean of IWC at around 100 hPa for SMILES (bands A, B, and C), MLS-640 GHz, and CALIPSO-CALIOP data. CloudSat-CPR data is not shown because it is not sensitive to ice clouds at this pressure level. Again, the three data sets agree well in the IWC geographical pattern, with high values in the ITCZ. As for pIWP, SMILES IWC is around 100% smaller/greater than the MLS and CALIPSO-CALIOP data, respectively, depending on location.

#### 4. Cloud Ice Water Path Diurnal Variation

[36] To further explore this new data set, the entire pIWP data was binned by time and separated into land and open ocean regimes to study their respective ice cloud diurnal variations. This diurnal variation is linked to the diurnal variation of cloudiness, deep convection and humidity, with all these diurnal cycles associated with the 24 h variation of the solar forcing. As such, these are fundamental components of the variability of the global climate system.

[37] Many studies have shown that over land, these diurnal cycles peak in the afternoon and early evening while, over the ocean, they peak around the early morning [e.g., Janowiak *et al.*, 1994; Chen and Houze, 1997; Tian *et al.*, 2004; Hong *et al.*, 2006; Yang *et al.*, 2001; Eriksson *et al.*, 2010]. Figure 11 shows the land and open ocean regimes used in this study as well as their respective diurnal deviation from the mean.

[38] As can be seen, there is a pronounced diurnal cycle over land peaking strongly in the afternoon/early evening. The timing of its maximum is similar to those of deep convective clouds and high cold clouds reported, either for tropical South Africa, tropical South America, or Australia, by Hong *et al.* [2006]. These cycles were derived with the Tropical Rainfall Measuring Mission (TRMM) Precipitation Radar (PR), e.g., [Kummerow *et al.*, 1998] and by the Visible and Infrared Scanner (VIRS). Over the open ocean, SMILES data show little temporal dependence and a multipeak structure.

#### 5. Data File Format

[39] All the SMILES IWC and pIWP data described here are available from <ftp://mls.jpl.nasa.gov/pub/outgoing/smiles>. The data are stored in the standard HDF version 5 on a one-day granularity, and named according to SMILES\_icecloud\_YYYY-mm-dd\_vXX\_XX.h5, where YYYY, mm, and dd are the calendar year, month and day, respectively, and where XX\_XX is the version number. Each file contains two swaths, IWC and pIWP and each of them contains three more swaths “A”, “B”, and “C”, which correspond to the data obtained from each of the SMILES bands.

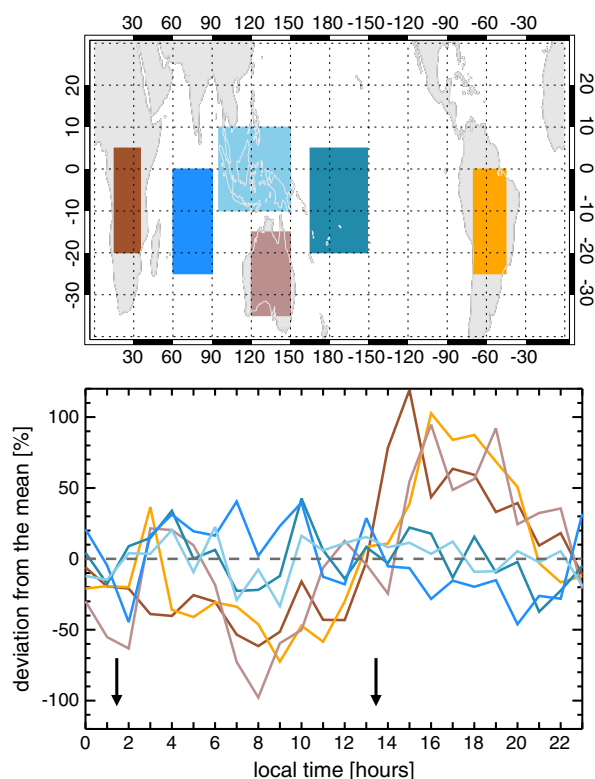


**Figure 11.** (top) Regions used to study the diurnal cycle of pIWP. (bottom) pIWP diurnal variation about 12.5 km over land (brown colors) and oceans (blue colors) as measured by SMILES. A combination of measurements from the three SMILES bands for the entire mission was used. The arrows indicate the temporal sampling of MLS, CloudSat and CALIPSO to highlight how much cloud variability is missed by these instruments.



[40] Each of these A/B/C swaths contains data fields called “val” and “precision”, which describe the value and the precision of the data, either in  $\text{mg/m}^3$  for IWC, or in  $\text{g/m}^2$  for pIWP. In addition to these fields, the geolocation information is given by the fields “latitude” and “longitude”; the universal time and date are given by the fields “ut” and “date”; and the local time and local date are saved in the fields, “localtime” and “localdate”.

[41] Furthermore, the IWC and RHi swaths include the field “pressure” in hPa, which indicates the pressure surface of the measurement. The RHi field also contains temperature in kelvins, water vapor and water vapor precision in ppmv and radiance  $\chi^2$  (chisq) fit value. In the near future, there will be another SMILES upper troposphere - lower stratosphere (UTLS) humidity product developed by the SMILES level-2 research processor in the National Institute of Information and Communications Technology (NICT).

[42] In addition to all these fields, each of the A/B/C swaths contain a “status” field. This is merely a flag indicating if that specific SMILES band was used that particular day. Values of “status” equal to zero indicate that there is no data in that swath.

## 6. Summary and Discussions

[43] After retrieving  $\text{O}_3$ , HCl, pressure, and RHi, we have estimated the clear-sky radiance for the entire SMILES mission. This clear-sky radiance is simply the forward model run, using GEOS-5 temperature, the previously retrieved  $\text{O}_3$ , HCl, pressure, and RHi values, but truncating the RHi at a value of 110%. Once the clear-sky radiance was known, we subtracted it from the measured radiances to compute the Tcir.

[44] These Tcir were mapped onto pIWP or IWC using Tcir-pIWP or Tcir-IWC relationships found using simulations of the 2-D Cloud-Sky Radiative Transfer model. These simulations were driven with a CloudSat-CPR and CALIPSO-CALIOP IWC merged fields, and the nearest MLS temperature and gas concentrations conditions. pIWP was derived from mostly negative Tcir measured between 1000 hPa and 180 hPa, while IWC was derived from 100 hPa to 70 hPa from mostly positive cloud induced radiances. Between these pressure ranges, the lack of contrast between clouds and the clear-sky background makes any cloud information difficult to infer. Systematic uncertainties affecting these products were investigated; the total systematic error was found to vary from 50% to 110% depending on the tangent pressure.

[45] pIWP and IWC visual inspection comparisons with the MLS, CloudSat-CPR, and CALIPSO-CALIOP data sets were found to agree well in the geographical pattern, displaying relatively high values in the ITCZ. Although no exact agreement was found in the magnitude with SMILES pIWP and IWC smaller/greater than the MLS, CloudSat-CPR and CALIPSO-CALIOP data, depending on the location, this was somewhat expected due to the different particle size sensitivity of each instrument, the different assumptions in each retrieval, and the diurnal nature of the SMILES data.

[46] After the pIWP was binned by time and region, the diurnal deviation from the mean was computed for land and open ocean conditions. Over land, the expected

diurnal variation was found with a pronounced diurnal variation peaking strongly in the afternoon/early evening. Over the open ocean, little temporal dependence was found.

[47] This data set is publicly available for download in HDF5 format. Future analysis of this data set, in combination with other observations such as the TRMM precipitation radar, can greatly improve our understanding of diurnal variations of cloud properties.

[48] **Acknowledgments.** The research described in this paper was carried out by the Jet Propulsion Laboratory, California Institute of Technology, under contract with the National Aeronautics and Space Administration. JEM/SMILES mission is a joint project of Japan Aerospace Exploration Agency (JAXA) and National Institute of Information and Communications Technology (NICT).

## References

- Baran, A. J. (2012), From the single-scattering properties of ice crystals to climate prediction: A way forward, *Atmos. Res.*, **112**, 45–69.
- Buehler, S. A., P. Eriksson, T. Kuhn, A. von Engel, and C. Verdes (2005), ARTS, the atmospheric radiative transfer simulator, *J. Quant. Spectrosc. Radiat. Transfer*, **91**, 65–93.
- Buehler, S. A., et al. (2007), A concept for a satellite mission to measure cloud ice water path, ice particle size, and cloud altitude, *Q. J. R. Meteorol. Soc.*, **133**(S2), 109–128.
- Buehler, S. A., et al. (2012), Observing ice clouds in the submillimeter spectral range: The CloudIce mission proposal for ESAs Earth Explorer 8, *Atmos. Meas. Tech.*, **5**, 1529–1549.
- Chen, S., and R. A. Houze (1997), Diurnal variation and life-cycle of deep convective systems over the tropical Pacific warm pool, *Q. J. R. Meteorol. Soc.*, **123**, 357–388.
- Cotton, R. J., P. R. Field, Z. Ulanowski, P. H. Kaye, E. Hirst, R. S. Greenaway, I. Crawford, J. Crosier, and J. Dorsey (2012), The effective density of small ice particles obtained from in situ aircraft observations of mid-latitude cirrus, *Q. J. R. Meteorol. Soc.*, doi:10.1002/qj.2058.
- Del Genio, A. D. (2001), *CGM Simulations of Cirrus for Climate Studies. Chapter 15 in Cirrus*, pp. 310–326, Oxford University Press, New York.
- Donovan, D., and A. Lammeren (2002), First ice cloud effective particle size parameterization based on combined lidar and radar data, *Geophys. Res. Lett.*, **29**(1), 1006, doi:10.1029/2001GL013731.
- Evans, K. F., S. J. Walter, A. J. Heymsfield, and M. N. Deeter (1998), Modeling of submillimeter passive remote sensing of cirrus clouds, *J. Appl. Meteorol.*, **37**, 184–205.
- Eriksson, P., M. Erkström, B. Rydberg, and D. P. Murtagh (2007), First Odin sub-mm retrievals in the tropical upper troposphere: Ice cloud properties, *Atmos. Chem. Phys.*, **7**, 471–483.
- Eriksson, P., B. Rydberg, M. Johnston, D. P. Murtagh, H. Struthers, S. Ferrachat, and U. Lohmann (2010), Diurnal variations of humidity and ice water content in the tropical troposphere, *Atmos. Chem. Phys.*, **10**, 11519–11533.
- Eriksson, P., S. A. Buehler, C. P. Davis, C. Emde, and O. Lemke (2011a), ARTS, the atmospheric radiative transfer simulator, version 2, *J. Quant. Spectrosc. Radiat. Transfer*, **112**, 1551–1558.
- Eriksson, P., B. Rydberg, and S. A. Buehler (2011b), On cloud ice induced absorption and polarisation effects in microwave limb sounding, *Atmos. Meas. Tech.*, **4**, 1305–1318.
- Field, P. R., A. J. Heymsfield, and A. Bansemer (2006), Shattering and particle interarrival times measured by optical array probes in ice clouds, *Am. Meteorol. Soc.*, **23**, 1357–1371.
- Field, P. R., A. J. Heymsfield, and A. Bansemer (2007), Snow size distribution parametrization for midlatitude and tropical ice cloud, *J. Atmos. Sci.*, **64**, 4346–4364.
- Heymsfield, A., A. Bansemer, P. R. Field, S. L. Durden, J. L. Stith, J. E. Dye, W. Hall, and C. A. Grainger (2002), Observations and parameterizations of particle size distributions in deep tropical cirrus and stratiform precipitating clouds: Results from in situ observations in TRMM field campaigns, *J. Atmos. Sci.*, **59**, 3457–3491.
- Hong, G., G. Heygster, and C. A. Morales Rodriguez (2006), Effect of cirrus clouds on the diurnal cycle of tropical deep convective clouds, *J. Geophys. Res.*, **111**, D06209, doi:10.1029/2005JD006208.
- IPCC (2007), Changes in atmospheric constituents and in radiative forcing, in *Climate Change 2007: The Physical Science Basis. Contribution of Working Group I to the Fourth Assessment Report of the Intergovernmental Panel on Climate Change*, edited by Solomon, S., D. Qin, M. Manning, Z. Chen, M. Marquis, K. B. Averyt, M. Tignor, and H. L.

- Miller, Cambridge University Press, Cambridge, United Kingdom and New York, NY, USA.
- Janoiwak, J. E., P. A. Arkin, and M. Morrisey (1994), An examination of the diurnal cycle in oceanic tropical rainfall using satellite and in situ data, *Mon. Weather Rev.*, **122**, 2296–2311.
- Jiang, J. H., et al. (2012), Evaluation of cloud and water vapor simulations in IPCC AR5 climate models using NASA A-Train satellite observations, *J. Geophys. Res.*, **117**, D14105, doi:10.1029/2011JD017237.
- Jiménez, C., S. A. Buehler, B. Rydberg, P. Eriksson, and K. F. Evans (2007), Performance simulations for a submillimetre-wave satellite instrument to measure cloud ice, *Q. J. R. Meteorol. Soc.*, **133**(S2), 129–149.
- Korolev, A. V., E. F. Emery, J. W. Strapp, S. G. Cober, G. A. Isaac, M. Wasey, and D. Marcotte (2011), Small ice particles in tropospheric clouds: Fact or artifact? Airborne icing instrumentation evaluation experiment, *Bull. Am. Meteorol. Soc.*, **92**, 967–973.
- Kikuchi, K., et al. (2010), Overview and early results of the Superconducting SubmillimeterWave Limb Emission Sounder (SMILES), *J. Geophys. Res.*, **115**, D23306, doi:10.1029/2010JD014379.
- Kumagai, H., H. Kuroiwa, S. Kobayashi, and T. Orikasa (2003), Cloud profiling radar for EarthCARE mission, *Proceedings of SPIE 4894, Microwave Remote Sensing of the Atmosphere and Environment III*, 118–125, Hangzhou, China.
- Kummerow, C., W. Barnes, T. Kozu, J. Shiue, and J. Simpson (1998), The tropical rainfall measuring mission (TRMM) sensor package, *J. Atmos. Oceanic Technol.*, **15**, 809–817.
- Lee, M.-I., S. D. Schubert, M. J. Suarez, J.-K. E. Schemm, H.-L. Pan, J. Han, and S.-H. Yoo (2008), Role of convection triggers in the simulation of the diurnal cycle of precipitation over the United States Great Plains in a general circulation model, *J. Geophys. Res.*, **113**, D02111, doi:10.1029/2007JD008984.
- Li, J.-L., et al. (2005), Comparisons of EOS MLS cloud ice measurements with ECMWF analyses and GCM simulations: Initial results, *Geophys. Res. Lett.*, **32**, L18710, doi:10.1029/2005GL023788.
- Li, J.-L., et al. (2012), An observationally based evaluation of cloud ice water in CMIP3 and CMIP5 GCMs and contemporary reanalyses using contemporary satellite data, *J. Geophys. Res.*, **117**, D16105, doi:10.1029/2012JD017640.
- Livesey, N., W. V. Snyder, W. G. Read, and P. Wagner (2006), Retrieval algorithms for the EOS Microwave Limb Sounder (MLS), *IEEE Trans. Geosci. Remote Sens.*, **44**(5), 1144–1155.
- Livesey, N. J., et al. (2011), EOS Aura MLS Version 3.3 Level 2 data quality and description document, *Technical Report D-33509*, Jet Propulsion Laboratory, California Institute of Technology.
- List, R. J., (1951), *Smithsonian Meteorological Tables*, pp. 347–385, Smithsonian Misc. Collect. 114, Smithsonian Institution, Washington, D.C.
- Manabe, T., T. Fukami, T. Nishibori, K. Mizukoshi, and S. Ochiai (2008), Measurement and evaluation of submillimeterwave antenna quasi-optical feed system by a phaseretrieval method in the 640 GHz band, *IEICE Trans. Comm.*, **E91-B**(6), 1760–1766.
- Manabe, T., T. Nishibori, K. Mizukoshi, F. Ohtsubo, and S. Ochiai (2010), Measurements of the offset Cassegrain antenna of JEM/SMILES using a nearfield phaseretrieval method in the 640 GHz band, paper presented at 21st International Symposium Space Terahertz Technology, Oxford, U.K., March 23–25, 2010.
- McFarquhar, G. M., and A. J. Heymsfield (1997), Parameterization of tropical cirrus ice crystal size distribution and implications for radiative transfer: Results from CEPEX, *J. Atmos. Sci.*, **54**, 2187–2200.
- Mishchenko, M. I., and L. D. Travis (1998), Capabilities and limitations of a current Fortran implementation of the T-matrix method for randomly oriented, rotationally symmetric scatterers, *J. Quant. Spectrosc. Radiat. Transfer*, **60**(3), 309–324.
- Mitchell, D. L., P. Rasch, D. Ivanova, G. McFarquhar, and T. Nousiainen (2008), Impact of small ice crystal assumptions on ice sedimentation rates in cirrus clouds and GCM simulations, *Geophys. Res. Lett.*, **35**, L09806, doi:10.1029/2008GL033552.
- Penner, J. E. (2004), The cloud conundrum, *Nature*, **432**, 962–963.
- Read, W. G., et al. (2001), UARS microwave limb sounder upper tropospheric humidity measurement: Method and validation, *J. Geophys. Res.*, **106**(D23), 32207–32258.
- Rienecker, M. M., et al. (2008), The GEOS-5 data assimilation system: A documentation of GEOS-5.0, *NASA/TM2008104606*, 27, 1–101.
- Rodgers, C. (2000), *Inverse Methods for Atmospheric Sounding: Theory and Practice*, Series on Atmospheric, Oceanic and Planetary Physics, vol. 2, pp. 1–236, World Scientific, Singapore.
- Stephens, G. L., S. Tsay, Jr. Stackhouse, and P. J. Flatau (1990), The relevance of the microphysical and radiative properties of cirrus clouds to climate and climatic feedback, *J. Atmos. Sci.*, **47**(14), 1742–1753.
- Stephens, G. L., et al. (2002), The Cloudsat mission and the A-train. A new dimension of space-based observations of clouds and precipitation, *Bull. Am. Meteorol. Soc.*, **83**, 1771–1790.
- Tian, B., B. J. Soden, and X. Wu (2004), Diurnal cycle of convection, clouds, and water vapor in the tropical upper troposphere: Satellites versus a general circulation model, *J. Geophys. Res.*, **109**, D10101, doi:10.1029/2003JD004117.
- Waters, J., et al. (2006), The Earth Observing System Microwave Limb Sounder (EOS MLS) on the Aura satellite, *IEEE Trans. Geosci. Remote Sens.*, **44**, 5.
- Wilheit, T. T., A. T. C. Chang, J. L. King, E. B. Rodgers, R. A. Nieman, B. M. Krupp, A. S. Milman, J. S. Stratigos, and H. Siddalingaiah (1982), Microwave radiometric observations near 19.35, 95 and 183 GHz of precipitation in tropical storm Cora, *J. Appl. Meteorol.*, **21**, 1137–1145.
- Wilson, D. (2000), The impact of a physically based microphysical scheme on the climate simulation of the Meteorological Office Unified Model, *Q. J. R. Meteorol. Soc.*, **126**, 1281–1300.
- Winker, D. M., M. A. Vaughan, A. Omar, Y. Hu, K. A. Powell, Z. Liu, W. H. Hunt, and S. A. Young (2009), Overview of the CALIPSO Mission and CALIOP data processing algorithms, *Bull. Am. Meteorol. Soc.*, **26**, 2310–2323.
- Wu, D. L., W. G. Read, A. E. Dessler, S. C. Sherwood, and J. H. Jiang (2005), UARS/MLS cloud ice measurements: Implications for H<sub>2</sub>O transport near the tropopause, *J. Atmos. Sci.*, **62**, 518–530.
- Wu, D. L. (2006), EOS MLS cloud ice measurements and cloud-sky radiative transfer model, *IEEE Trans. Geosci. Remote Sens.*, **44**(5), 1156–1165.
- Wu, D. L., J. H. Jiang, W. G. Read, R. T. Austin, C. P. Davis, A. Lambert, G. L. Stephens, D. G. Vane, and J. W. Waters (2008), Validation of the Aura MLS cloud ice water content measurements, *J. Geophys. Res.*, **113**, D15S10, doi:10.1029/2007JD008931.
- Yang, G.-Y., and J. Slingo (2001), The diurnal cycle in the tropics, *Mon. Weather Rev.*, **129**, 784–801.
- Yeh, H. M., N. Prasad, R. A. Mack, and R. F. Adler (1990), Aircraft microwave observations and simulation of deep convection from 18 to 183 GHz. Part II: Model results, *J. Atmos. Oceanic Technol.*, **7**, 392–410.